Interplay of space charge and intrabeam scattering in the LHC ion injector chain

M. Zampetakis*
European Organization for Nuclear Research (CERN), CH-1211 Geneva 23, Switzerland; and
Department of Physics, University of Crete, P.O. Box 2208, GR-71003 Heraklion, Greece

F. Antoniou, F. Asvesta, H. Bartosik, and Y. Papaphilippou
European Organization for Nuclear Research (CERN), CH-1211 Geneva 23, Switzerland;

A. Saá Hernández
Instituto Galego de Física de Altas Enerxías (IGFAE),
Universidade de Santiago de Compostela, Santiago de Compostela, Spain

The ion injectors of the CERN accelerator chain, in particular the Super Proton Synchrotron (SPS) and the Low Energy Ion Ring (LEIR), operate in a strong space charge (SC) and intrabeam scattering (IBS) regime, which can degrade beam quality. Optimizing the ion beam performance requires thus to study the interplay of these two effects in tracking simulations by incorporating both SC and IBS effects interleaved with lattice nonlinearities. In this respect, the kinetic theory approach of treating IBS effects has been deployed. A new, modified approach has been introduced using the formalism of the Bjorken and Mtingwa model and the complete elliptic integrals of the second kind for faster numerical evaluation. This IBS kick is implemented in PyORBIT and extensive benchmarking cases against analytical models are shown. Results of combined space charge and intra-beam scattering simulations for the SPS and LEIR are presented and compared with observations from beam measurements.

I. INTRODUCTION

Incoherent effects like Intrabeam Scattering (IBS) and Space Charge (SC) can significantly limit the beam performance of hadron synchrotrons and have therefore been intensively studied in several accelerators and regimes. In particular, IBS plays an important role in ion and proton storage rings, in which the beam is stored for many hours [1–7], in damping rings, light sources and linear accelerators [8–16] and in very low energy ion machines [17–19]. On the other hand, SC effects have been studied in many low-energy machines [20–31] and damping rings [32–35], as the SC induced tune shift can result in particle losses and transverse emittance increase due to periodic resonance crossing.

The interplay between IBS and SC can further enhance particle diffusion in phase space in the presence of excited resonances, as was shown in simulation studies for the Compact LInear Collider Damping Rings (CLIC DRs) [36]. In rings, that operate below the transition energy, IBS can lead to emittance exchange between the longitudinal and the transverse planes. This mechanism could not be simulated with the simplified IBS kick implemented in the tracking simulations described in Refs. [4, 36]. Thus, a more general implementation of the IBS kick is required to take into account the exchange of momenta in all planes.

The most commonly used numerical method for simulating the three-dimensional IBS effects is the "binary collisions" model (BCM). In this model, a distribution of macroparticles is divided into cells and each macroparticle is considered to interact with any other neighboring macroparticle during a specific time window. The probability of this interaction depends on the macroparticle density in each specific cell. The BCM model is implemented in various tracking codes, e.g. the MOnte-CArlo Code (MOCAC) [37], the Software for IBS and Radiation Effects (SIRE) [38] and the IBStrack [39] found in the collective effects simulation tool CMAD [40, 41]. Some of these codes include other effects like electron cooling and radiation damping as well.

The downside of the BCM model is that a large number of macroparticles is required (typically $> 5 \times 10^4$) in order to have sufficiently populated cells. In the case of turn-by-turn calculations in the presence of additional dynamical effects, this translates to a high demand on computational resources. To overcome this challenge, a three-dimensional approximate model (AM) was introduced in the past [42–44], rising from the general Kinetic Theory of gases. This model is based on the Fokker-Planck partial differential Equation (FPE) that describes the evolution over time of the probability density function of the velocity of a particle that experiences friction and random forces [45].

To progress in the understanding of the performance limitations of the heavy ion injector chain at CERN, it is important to have a reliable tool to simulate IBS together with other effects. Such a simulation tool will also be crucial for studies of future collider projects. In [36], a simple kick was used to simulate the IBS effect in tracking simulations for rings that operate above transition where no equilibrium can exist [46]. This means that all three planes growth indefinitely in the presence of IBS alone, if no other limitations are exceeded. However, for rings operating below transition, equilibrium among the three planes can exist. Thus, simulating the IBS effect entails the additional complexity that the momenta exchange due to IBS can lead to damping of the emittance in one or more planes [46]. In this case, a simple diffusive kick is not sufficient and a friction force is needed to simulate the particle' momenta exchange. In this paper, we introduce a general IBS kick based on the Kinetic Theory [42–44] and the Nagaitsev's

* michail.zampetakis@cern.ch

formalism [47], which is capable of dealing with rings that operate below transition as well. Using this kick, a simulation campaign was performed for the CERN ion injectors, in particular the Low Energy Ion Ring (LEIR) and the Super Proton Synchrotron (SPS). The goal of these simulations is to understand and recreate experimental observations of transverse emittance growth, that so far could not be explained by standalone IBS and SC simulations, by studying the interplay between SC and IBS.

This paper is organized in the following way. After this Introduction, in Sec. II, the analytical model of Bjorken and Mtingwa [48] will be recaptured. Their formalism will be useful in Sec. III where the Kinetic Theory approach and the approximate model introduced in [42–44] will be recalled. Then, our generalized and simplified IBS kick will be discussed in detail using both the formalism of Bjorken and Mtingwa [48] and the formalism of Nagaitsev [47], which uses the complete elliptic integrals of the second kind. In Sec. IV, the simulation setup will be discussed and a thorough benchmarking of the introduced IBS kick will be shown for different configurations in LEIR as well as the SPS. Section V summarizes the study case of LEIR. First the operational aspects of LEIR are discussed. Then, stand-alone tracking simulations with SC and IBS, as well as combined SC and IBS simulations are shown. Similarly, in Sec. VI, a case for the SPS is presented where beam measurements are compared with tracking simulations in the presence of the two effects. The main conclusions of this work are presented in Sec. VII.

II. THE BJORKEN AND MTINGWA FORMALISM

After the classical IBS model of Piwinski [46], Bjorken and Mtingwa (BM) came up with a quantum model [48] to analytically estimate the effect that IBS has in beams of charged particles. Their model is based on the Fermi's relativistic "Golden Rule" for the transition rate due to a 2-body scattering process and includes the effect of strong-focusing lattices.

In the BM model, all that is needed to characterize the emittance growth rates due to IBS are the auxiliary matrices $L^{(x)}$, $L^{(y)}$, $L^{(z)}$. After some years, these matrices have been generalized to include non-relativistic factors and vertical dispersion [49, 50]. The updated matrices are given by:

$$L^{(x)} = \begin{pmatrix} \frac{\beta_x}{\varepsilon_x} & -\gamma\phi_x\frac{\beta_x}{\varepsilon_x} & 0 \\ -\gamma\phi_x\frac{\beta_x}{\varepsilon_x} & \gamma^2\frac{\mathcal{H}_x}{\beta_x} & 0 \\ 0 & 0 & 0 \end{pmatrix}, \tag{1}$$

$$L^{(y)} = \begin{pmatrix} 0 & 0 & 0 \\ 0 & \gamma^2\frac{\mathcal{H}_y}{\beta_y} & -\gamma\phi_y\frac{\beta_y}{\varepsilon_y} \\ 0 & -\gamma\phi_y\frac{\beta_y}{\varepsilon_y} & \frac{\beta_y}{\varepsilon_y} \end{pmatrix}, \tag{2}$$

$$L^{(z)} = \begin{pmatrix} 0 & 0 & 0 \\ 0 & \frac{\gamma^2}{\sigma_\delta^2} & 0 \\ 0 & 0 & 0 \end{pmatrix}. \tag{3}$$

The sum of these three matrices gives the general auxiliary matrix L, defined as:

$$L = \begin{pmatrix} \frac{\beta_x}{\varepsilon_x} & -\gamma\phi_x\frac{\beta_x}{\varepsilon_x} & 0 \\ -\gamma\phi_x\frac{\beta_x}{\varepsilon_x} & \gamma^2(\frac{\mathcal{H}_x}{\beta_x}+\frac{\mathcal{H}_y}{\beta_y}+\frac{1}{\sigma_\delta^2}) & -\gamma\phi_y\frac{\beta_y}{\varepsilon_y} \\ 0 & -\gamma\phi_y\frac{\beta_y}{\varepsilon_y} & \frac{\beta_y}{\varepsilon_y} \end{pmatrix}, \tag{4}$$

where γ is the Lorentz factor, $\varepsilon_{x,y}$ are the transverse emittances, σ_δ is the momentum spread, $\beta_{x,y}$ are the beta functions of the lattice, $\eta_{x,y}$, $\eta'_{x,y}$ the dispersion function with its derivative and $\phi_{x,y}$, $\mathcal{H}_{x,y}$ are functions of the optics parameters and are given by the following expressions:

$$\phi_{x,y} = \eta'_{x,y} - \frac{\beta'_{x,y}\eta_{x,y}}{2\beta_{x,y}}, \tag{5}$$

$$\mathcal{H}_{x,y} = \frac{1}{\beta_{x,y}}\left[D_{x,y}^2 + \left(\beta_{x,y}\eta'_{x,y} - \frac{1}{2}\beta'_{x,y}\eta_{x,y}\right)^2\right]. \tag{6}$$

The growth rates can be expressed through the diffusion kernels $I_{ij}^B M$ (K_{ij} in [48]), defined as:

$$I_{ij}^{\mathrm{BM}} = \frac{A_{\mathrm{BM}}}{4\pi}\int\frac{d^3\theta e^{-\theta_i\theta_j L_{ij}/4}}{\theta^3}(\delta_{ij}\theta^2 - 3\theta_i\theta_j), \tag{7}$$

with θ_i being the scattering angle in plane i, and the constant A_{BM} defined as:

$$A_{\mathrm{BM}} = \frac{cNr_0^2}{8\pi\beta^3\gamma^4\varepsilon_x\varepsilon_y\sigma_z\sigma_\delta}C_{\log}, \tag{8}$$

where $C_{\log}$ is the Coulomb logarithm, β and γ are the relativistic parameters, c is the speed of light in vacuum and r_0 is the classical radius of the particle.

To make the integral expressions simpler, the kernels can be expressed explicitly in terms of the tensor $\mathscr{L} = L + \lambda I$, with I the unit matrix, following [48]:

$$I_{ij}^{\mathrm{BM}} = A_{\mathrm{BM}}\int_0^\infty\frac{d\lambda\,\lambda^{1/2}}{\sqrt{\det\mathscr{L}}}(\delta_{ij}Tr\mathscr{L}^{-1} - 3\mathscr{L}_{i,j}^{-1}). \tag{9}$$

Then, the growth rates are given by the the summation of the diffusion kernels and the auxiliary matrices $L^{(i)}$ with $i = x, y, z$ from the formula:

$$\frac{1}{T_{x,y,z}} = \sum_{ij} I_{ij}^{\mathrm{BM}} L_{ij}^{(x,y,z)}, \tag{10}$$

which, if we simply extend the summation, leads to the following expressions for the growth rates in each plane:

$$\frac{1}{T_x} = \left\langle\frac{\beta_x}{\varepsilon_x}I_{xx}^{\mathrm{BM}} - 2\gamma\frac{\beta_x\phi_x}{\varepsilon_x}I_{xz}^{\mathrm{BM}} + \gamma^2\frac{\mathcal{H}_x}{\varepsilon_x}I_{zz}^{\mathrm{BM}}\right\rangle, \tag{11}$$

$$\frac{1}{T_y} = \left\langle \frac{\beta_y}{\varepsilon_y} I_{yy}^{\mathrm{BM}} - 2\gamma \frac{\beta_y \phi_y}{\varepsilon_y} I_{yz}^{\mathrm{BM}} + \gamma^2 \frac{\mathcal{H}_y}{\varepsilon_y} I_{zz}^{\mathrm{BM}} \right\rangle, \tag{12}$$

$$\frac{1}{T_z} = \left\langle \frac{\gamma^2}{\sigma_\delta^2} I_{zz}^{\mathrm{BM}} \right\rangle, \tag{13}$$

where the brackets denote averaging around the ring circumference.

III. KINETIC KICK

Following [42–44], we introduce the vector $\vec{r}$ and the dimensionless momentum vector $\vec{p}$

$$\vec{r} = \begin{pmatrix} z - z_s \\ x \\ y \end{pmatrix}, \qquad \vec{p} = \begin{pmatrix} \frac{1}{\gamma}\frac{\Delta p}{p} \\ x' \\ y' \end{pmatrix}, \tag{14}$$

with z being the longitudinal particle coordinate, z_s the longitudinal coordinate of the bunch center, x and y the horizontal and vertical transverse coordinates, p the particle momentum, Δp its deviation from the equilibrium value and $x' = p_x/p$, $y' = p_y/p$ (p_x, p_y being the horizontal and vertical momentum components). The FPE in phase space has the following form (summation over indices m and m'):

$$\frac{\partial \Phi}{\partial t} = -\frac{\partial}{\partial p_m}(F_m \Phi) + \frac{1}{2}\frac{\partial^2}{\partial p_m \partial p_{m'}}(D_{m,m'}\Phi). \tag{15}$$

Here Φ is the distribution function in phase space, F_m are the components of the friction force $\vec{F}$, $D_{m,m'}$ are the diffusion coefficients. Both the friction and diffusion coefficients depend on the Twiss parameters of the ring and the beam parameters, making their evaluation an arduous procedure. To simplify the model, the components of the friction force are considered to be a linear function of the momentum $F_m = -K_m p_m$ with constant coefficients K_m, and all components of the diffusion tensor are considered constant. Furthermore, it is assumed that most of the IBS interactions take place inside the beam core, which is usually similar to a Gaussian distribution.

Averaging over all particles and following the aforementioned approximations of the AM model [42, 44], the friction and diffusion coefficients are given by the following expressions:

$$K_i = \frac{A_{\mathrm{BM}}}{\left\langle p_i^2 \right\rangle} \mathcal{I}_{i,i}, \tag{16}$$

$$D_{i,j} = A_{\mathrm{BM}} \left(\delta_{ij} \sum_{k=1}^{3} \mathcal{I}_{k,k} - \mathcal{I}_{i,j} \right). \tag{17}$$

In the AM model, it is assumed that $\left\langle p_x^2 \right\rangle = \varepsilon_x/\beta_x$, $\left\langle p_y^2 \right\rangle = \varepsilon_y/\beta_y$ and $\left\langle p_z^2 \right\rangle = \sigma_\delta^2$. The integrals $\mathcal{I}_{i,j}$ are given by:

$$\mathcal{I}_{i,j} = \int \frac{d^3\theta e^{-\theta_i \theta_j L_{i,j}/4}}{\theta^3} \theta_i \theta_j. \tag{18}$$

Further derivations and formalisms for the coefficients and the integrals of this model are neglected here since they are out of the scope of this paper.

In order to simulate the IBS effect in a particle distribution, the momentum kick to be applied to each particle is being derived by the Langevin Equation (LE):

$$p_i(t + \Delta t) = p_i(t) - K_i p_i(t)\Delta t + \sqrt{\Delta t} \sum_{j=1}^{3} C_{i,j} \varsigma_j, \tag{19}$$

where ς_j are three random numbers with Gaussian distribution and unity standard deviation, and the coefficients $C_{i,j}$ are functions of the friction and diffusion coefficients, taking into account correlations between coupled transverse and longitudinal degrees of freedom. The $C_{i,j}$ are the coefficients of a 3×3 matrix which can be found by solving the equations derived by averaging over the possible values of the random numbers ς_j and over the test and field particles, as shown in [42].

A. Modified Approximate Model

The AM was benchmarked successfully against the BCM for the TWAC storage ring [42]. On the other hand, for the CERN Ion injectors, the simulation results obtained with the AM model [42, 44] were significantly different from the expected results, especially in the horizontal plane, when comparing to the results obtained by other analytical models like BM [48], or the method of Nagaitsev [47].

Inspired by the AM method and following the same main structure of the theory, an alternative approach was implemented, including vertical dispersion as well. Instead of solving the system for the $C_{i,j}$ coefficients, a more general set of diffusion and friction coefficients was calculated. Following the same simplification steps of [48], as were used to derive Eq. (9) from Eq. (7), the friction and diffusion coefficients of Eqs. (16, 17), respectively, can be rewritten as:

$$K_i = \frac{A_{\mathrm{BM}}}{\left\langle p_i^2 \right\rangle} \int_0^\infty d\lambda \, \frac{\lambda^{1/2}}{\sqrt{\det \mathscr{L}}} \mathscr{L}_{i,i}^{-1}, \tag{20}$$

$$D_{i,j} = A_{\mathrm{BM}} \int_0^\infty d\lambda \, \frac{\lambda^{1/2}}{\sqrt{\det \mathscr{L}}} (\delta_{ij} Tr \mathscr{L}^{-1} - \mathscr{L}_{i,j}^{-1}), \tag{21}$$

where again $\mathscr{L} = L + \lambda I$, with I the unit matrix. In this form, it is evident that the diffusion kernels I_{ij}^{BM} of Eq. (9) can be rewritten as a function of the friction and diffusion coefficients of Eqs. (20, 21), as follows:

$$I_{ij}^{\mathrm{BM}} = D_{i,j} - 2\delta_{ij} \left\langle p_i^2 \right\rangle K_i. \tag{22}$$

Substituting the diffusion kernels in the IBS growth rates given above with the diffusion and friction coefficients of the AM model using the relation of Eq. (22), leads to the following expressions:

$$G_x = \left\langle \frac{\beta_x}{\varepsilon_x} D_{x,x} - 2\gamma \frac{\beta_x \phi_x}{\varepsilon_x} D_{x,z} + \gamma^2 \frac{\mathcal{H}_x}{\varepsilon_x} D_{z,z} \right\rangle, \tag{23}$$

$$G_y = \left\langle \frac{\beta_y}{\varepsilon_y} D_{y,y} - 2\gamma \frac{\beta_y \phi_y}{\varepsilon_y} D_{y,z} + \gamma^2 \frac{\mathcal{H}_y}{\varepsilon_y} D_{z,z} \right\rangle, \tag{24}$$

$$G_z = \left\langle \frac{\gamma^2}{\sigma_\delta^2} D_{z,z} \right\rangle, \tag{25}$$

$$F_x = \left\langle 2K_x + 4\gamma \frac{\beta_x \phi_x}{\varepsilon_x} K_{x,z} - 2\gamma^2 \sigma_\delta^2 \frac{\mathcal{H}_x}{\varepsilon_x} K_z \right\rangle, \tag{26}$$

$$F_y = \left\langle 2K_y + 4\gamma \frac{\beta_y \phi_y}{\varepsilon_y} K_{y,z} - 2\gamma^2 \sigma_\delta^2 \frac{\mathcal{H}_y}{\varepsilon_y} K_z \right\rangle, \tag{27}$$

$$F_z = \left\langle 2\gamma^2 K_z \right\rangle, \tag{28}$$

where the expressions including diffusion and friction terms have been separated for each plane to $G_{x,y,z}$ and $F_{x,y,z}$, respectively. It should be emphasized that these coefficients have been derived based on the formalism of the BM model.

To apply the IBS kick to the momenta of each particle i in the distribution for each plane $u = x, y, z$ using the generalized G_u and F_u coefficients in place of the original diffusion and friction coefficients of the AM model (Eqs. (20, 21)), a modified LE is proposed in the following form:

$$p_u(t + \Delta t) = p_u(t) - F_u p_u(t) \rho(z) \Delta t + \sigma_{p_u} \sqrt{2 G_u \Delta t \rho(z)} \varsigma_u, \tag{29}$$

where ς_u is a random number following a normal distribution with zero mean and unit standard deviation, $\rho(z) = 2\sigma_z \sqrt{\pi} \lambda(z)$, where $\lambda(z)$ stands for the normalized longitudinal line density at position z within the bunch, and σ_z is the bunch length. Last, σ_{p_u} is the RMS momentum of plane u. For the transverse planes, the momenta $p_{x,y}$ have to be corrected in terms of the off-momentum position of each particle i, and the optics at the position of the kick, as

$$\tilde{p}_u^i = \left(p_u^i - \eta_u' \frac{\Delta p_i}{p_0} \right) \times \sqrt{\beta_u} + \left(u_i - \eta_u \frac{\Delta p_i}{p_0} \right) \times \frac{\alpha_u}{\sqrt{\beta_u}}, \quad u = x, y. \tag{30}$$

After applying the kick, the transverse momenta have to be converted back to the physical reference system with their corresponding off-momentum position.

The modified LE was inspired by the simple IBS kick that was first introduced to include the longitudinal line density [51, 52] that was later used for IBS studies [4, 36].

B. Using the complete elliptic integrals of the second kind

A limitation of long tracking simulations with many macroparticles comes usually from the required computing resources. Including collective effects with heavy computations, such as IBS, can further increase the processing power requirements. To make the calculations of the IBS growth rates more efficient, Nagaitsev [47] expressed the integrals of the BM model through closed-form expressions with the use of the complete, symmetric, elliptic integral of the second kind $R_D(x, y, z)$ (with the drawback of ignoring the vertical dispersion). Following Carlson's definition, this integral is given by

$$R_D(x, y, z) = \frac{3}{2} \int_0^\infty \frac{dt}{\sqrt{(t + x)(t + y)(t + z)^3}}, \tag{31}$$

and can be solved without the need of an approximation function. Instead, it relies on a very efficient integral calculation algorithm, based on the duplication theorem [53].

Following the formalism of Nagaitsev [47], the IBS growth rates can be expressed through the following three integrals:

$$R_1 = \frac{1}{\lambda_1} R_D\left(\frac{1}{\lambda_2}, \frac{1}{\lambda_3}, \frac{1}{\lambda_1} \right), \tag{32}$$

$$R_2 = \frac{1}{\lambda_2} R_D\left(\frac{1}{\lambda_3}, \frac{1}{\lambda_1}, \frac{1}{\lambda_2} \right), \tag{33}$$

$$R_3 = \frac{1}{\lambda_3} R_D\left(\frac{1}{\lambda_1}, \frac{1}{\lambda_2}, \frac{1}{\lambda_3} \right), \tag{34}$$

where $\lambda_1, \lambda_2, \lambda_3$ are the three eigenvalues of the auxiliary 3×3 matrix L, defined in the BM model [48], as was previously shown in Eq. (4). The three eigenvalues are given by:

$$\lambda_1 = a_y, \tag{35}$$

$$\lambda_2 = a_1 + q_x \tag{36}$$

$$\lambda_3 = a_1 - q_x \tag{37}$$

with

$$a_x = \frac{\beta_x}{\varepsilon_x}, \quad a_y = \frac{\beta_y}{\varepsilon_y}, \quad a_s = a_x \left(\frac{\eta_x^2}{\beta_x^2} + \phi_x^2 \right) + \frac{1}{\sigma_\delta^2}, \tag{38}$$

$$a_1 = \frac{1}{2}(a_x + \gamma^2 a_s), \quad a_2 = \frac{1}{2}(a_x - \gamma^2 a_s), \tag{39}$$

$$q_x = \sqrt{a_2^2 + \gamma^2 a_x^2 \phi_x^2}. \tag{40}$$

Here, the goal is to express the diffusion and friction coefficients of the AM model with the extension to our generalized model, through the same elliptic integrals of the Nagaitsev's formalism. For convenience, the friction and diffusion coefficients of the AM model given by Eqs. (20) and (21), respectively, are written as

$$K_i = \frac{A_N}{\left\langle p_i^2 \right\rangle} \Theta_{i,i}, \quad D_{i,j} = A_N \left(\delta_{ij} \sum_{k=1}^{3} \Theta_{k,k} - \Theta_{i,j} \right), \tag{41}$$

where A_N is the constant term preceding the integrals, following the formalism of Nagaitsev [47] and the integral $\Theta_{i,j}$ is defined as:

$$\Theta_{i,j} = \int_0^\infty d\lambda \, \frac{\lambda^{1/2}}{\sqrt{\det \mathscr{L}}} \mathscr{L}_{i,j}^{-1}. \tag{42}$$

Following the same procedure as before, the diffusion kernels I_{ij}^{BM} in the IBS growth rates given in Eqs. (11), (12) and (13) are substituted by the diffusion and friction coefficients of Eq. (41) using again the relation given by Eq. (22). This yields the following expressions:

$$\frac{1}{T_x} = \left\langle \frac{\beta_x}{\varepsilon_x}\left(\Theta_{y,y} + \Theta_{z,z} - 2\Theta_{x,x}\right) - 2\gamma\frac{\beta_x\phi_x}{\varepsilon_x}\Theta_{x,z} + \gamma^2\frac{\mathcal{H}_x}{\varepsilon_x}\left(\Theta_{x,x} + \Theta_{y,y} - 2\Theta_{z,z}\right)\right\rangle, \tag{43}$$

$$\frac{1}{T_y} = \left\langle \frac{\beta_y}{\varepsilon_y}\left(D_{y,y} - 2\langle p_y^2\rangle K_y\right)\right\rangle = \left\langle \frac{\beta_y}{\varepsilon_y}\left(\Theta_{x,x} + \Theta_{z,z} - 2\Theta_{y,y}\right)\right\rangle, \tag{44}$$

$$\frac{1}{T_p} = \left\langle \frac{\gamma^2}{\sigma_\delta^2}\left(\Theta_{x,x} + \Theta_{y,y} - 2\Theta_{z,z}\right)\right\rangle. \tag{45}$$

Comparing Eqs. (43), (44) and (45) with the partial IBS growth rates given by Eqs. (30), (31) and (32) in [47], yields the following system of equations that expresses the integrals $\Theta_{i,j}$ in terms of the elliptic integrals R_1, R_2 and R_3:

$$\Theta_{x,x} + \Theta_{z,z} = R_2 + R_3, \qquad \Theta_{y,y} = R_1, \tag{46}$$

$$\Theta_{x,x} = \frac{1}{2}\left[R_2\left(1 + \frac{a_2}{q_x}\right) + R_3\left(1 - \frac{a_2}{q_x}\right)\right], \tag{47}$$

$$\Theta_{z,z} = \frac{1}{2}\left[R_2\left(1 - \frac{a_2}{q_x}\right) + R_3\left(1 - \frac{a_2}{q_x}\right)\right], \tag{48}$$

$$\Theta_{x,z} = \frac{3\gamma^2\phi_x^2 a_x}{q_x}\left(R_3 - R_2\right), \tag{49}$$

where we defined $q_x = \sqrt{a_2^2 + \gamma^2 a_x^2\phi_x^2}$ to simplify the formulas.

Using these expressions, we can now reverse back to the initial diffusion and friction coefficients of AM, this time expressed in terms of the elliptic integrals R_1, R_2 and R_3. The new expressions are:

$$D_{x,x} = \frac{1}{2}\left[2R_1 + R_2\left(1 - \frac{a_2}{q_x}\right) + R_3\left(1 + \frac{a_2}{q_x}\right)\right], \tag{50}$$

$$D_{z,z} = \frac{1}{2}\left[2R_1 + R_2\left(1 + \frac{a_2}{q_x}\right) + R_3\left(1 - \frac{a_2}{q_x}\right)\right], \tag{51}$$

$$D_{x,z} = \frac{3\gamma^2\phi_x^2 a_x}{q_x}\left(R_3 - R_2\right), \tag{52}$$

$$K_x = \Theta_{x,x} = \frac{1}{2}\left[R_2\left(1 + \frac{a_2}{q_x}\right) + R_3\left(1 - \frac{a_2}{q_x}\right)\right], \tag{53}$$

$$K_z = \Theta_{z,z} = \frac{\gamma^2}{2}\left[R_2\left(1 - \frac{a_2}{q_x}\right) + R_3\left(1 + \frac{a_2}{q_x}\right)\right], \tag{54}$$

$$D_{y,y} = \Theta_{x,x} + \Theta_{z,z} = R_2 + R_3, \quad K_y = \Theta_{y,y} = R_1. \tag{55}$$

Following the same method, the new elliptic diffusion and friction coefficients are placed in Eqs. (11), (12) and (13) and separated to form the new $\tilde{G}_{x,y,z}$ and $\tilde{F}_{x,y,z}$ kick coefficients based on elliptic integrals, given by:

$$\tilde{G}_x = \frac{1}{\varepsilon_x}\frac{Nr_0^2 cC_{\log}}{12\pi\beta^3\gamma^5\sigma_z}\int_0^L \frac{\beta_x ds}{L\sigma_x\sigma_y}\left[D_{x,x} + \left(\frac{\eta_x^2}{\beta_x^2} + \phi_x^2\right)D_{z,z} + D_{x,z}\right], \tag{56}$$

$$\tilde{G}_y = \frac{1}{\varepsilon_y}\frac{Nr_0^2 cC_{\log}}{12\pi\beta^3\gamma^5\sigma_z}\int_0^L \frac{\beta_y ds}{L\sigma_x\sigma_y}D_{y,y}, \tag{57}$$

$$\tilde{G}_z = \frac{1}{\sigma_\delta^2}\frac{Nr_0^2 cC_{\log}}{12\pi\beta^3\gamma^5\sigma_z}\int_0^L \frac{ds}{L\sigma_x\sigma_y}D_{z,z}, \tag{58}$$

$$\tilde{F}_x = \frac{1}{\varepsilon_x}\frac{Nr_0^2 cC_{\log}}{12\pi\beta^3\gamma^5\sigma_z}\int_0^L \frac{\beta_x ds}{L\sigma_x\sigma_y}\left[K_x + \left(\frac{\eta_x^2}{\beta_x^2} + \phi_x^2\right)K_z\right], \tag{59}$$

$$\tilde{F}_y = \frac{1}{\varepsilon_y}\frac{Nr_0^2 cC_{\log}}{12\pi\beta^3\gamma^5\sigma_z}\int_0^L \frac{\beta_y ds}{L\sigma_x\sigma_y}K_y, \tag{60}$$

$$\tilde{F}_z = \frac{1}{\sigma_\delta^2}\frac{Nr_0^2 cC_{\log}}{12\pi\beta^3\gamma^5\sigma_z}\int_0^L \frac{ds}{L\sigma_x\sigma_y}K_z. \tag{61}$$

Note that the expressions for the coefficients $\tilde{F}_{x,y,z}$, $\tilde{G}_{x,y,z}$ are for a lattice element of length L. For the average coefficients, integration over the full circumference C of the ring is required, similar to most of the IBS models. It should be emphasized that the coefficients $\tilde{G}_i$ and $\tilde{F}_i$ have been derived using the formalism of the Nagaitsev method. To simulate the IBS effect for a coasting beam, the bunch length has to be replaced by $\sigma_z = C/2\sqrt{\pi}$ in these expressions and one has to consider that $T_p^{\mathrm{coasting}} = 2T_p^{\mathrm{bunched}}$ [46].

IV. SIMULATION SET-UP AND BENCHMARKING OF THE IBS MODEL

The simulations studies of the incoherent effects of SC and IBS were performed using the Polymorphic Tracking Code (PTC) [54] in the PyORBIT [55] simulation library. PyORBIT is a well-known simulation tool that has been intensively benchmarked and used for SC studies for many different accelerators [24, 56–60]. It provides the possibility to use various models for the SC potential, e.g. a fully self-consistent 2.5 D Particle-In-Cell (PIC) solver, a slice-by-slice SC solver and an analytical frozen potential solver.

For the presented studies, the SC effect is included using the SC frozen potential solver, where the SC kick at a given

position in the ring is analytically calculated from the lattice functions, the beam intensity and the transverse beam sizes using the Bassetti-Erskine formula [61]. This space charge kick is weighted by the line density at the longitudinal position of the particle being tracked. The kick is applied at multiple locations around the ring, known as SC nodes. A benchmarking case for the number of SC nodes used in the presented simulations can be found in Appendix A.

The term "frozen potential" in SC simulations refers to a model where the electrostatic potential generated by a bunch of charged particles is assumed to be static or "frozen", meaning it does not evolve as the beam parameters evolve. In studies that also account for excited resonances or IBS, the assumptions underlying the "frozen" space charge potential may no longer hold. In order to achieve a quasi self-consistent evaluation of the SC kick during the simulation run, the SC potential was recomputed every 500 turns according to the evolution of the transverse beam parameters and the longitudinal line density. This method is known as the "adaptive frozen model", which allows for a more accurate representation of dynamic effects while reducing noise effects from the limited number of macroparticles.

In order to perform the studies of the interplay between the incoherent effects of SC and IBS, an additional module was implemented inside PyORBIT. This module follows the formalism of the modified AM using the elliptic integrals of Nagaitsev, as described in the previous section. It was successfully benchmarked against analytical calculations for the LEIR and the SPS. In this paper, benchmarking cases for different parameter regimes in the LEIR and the SPS, with Pb-ions, will be presented. As performed for SC calculations, the IBS kick is applied once per turn. However, to make the IBS calculations more efficient, in all the benchmarking and study cases that will be shown here, the IBS kicks are re-evaluated every 500 turns according to the evolution of the transverse beam parameters and the longitudinal line density (as in the case of SC). The total duration of the simulation is 250000 turns, which is slightly shorter than the full cycle of the ring. The initial macroparticle distribution is initialized as Gaussian in the transverse planes. To reproduce the experimental observations, the initial longitudinal distribution is generated as a binomial distribution $g(x) = (1 - x^2)^{\mu}$ of exponent $\mu = 15$, which is not far from a Gaussian distribution.

Figure 1 shows the horizontal normalized emittance (blue), vertical normalized emittance (green) and the momentum spread (red) comparing the IBS kick from the modified AM (light colors) and the analytical predictions using Nagatisev's model (dark colors) for the nominal parameters of the LEIR, as described in Table I. The transverse emittances and the momentum spread are evaluated using the second-order moments of the macroparticle distribution, following a similar approach as described in [23]. In particular, a Gaussian fit is applied to the beam profile, and then the weighted RMS emittances are calculated from the actual beam profile up to the 8σ extent of the Gaussian fit. Excellent agreement is observed in all three planes.

To further benchmark the IBS kick, another benchmarking case was performed in the regime of a round beam with small

TABLE I. The LEIR Parameters

Ring and Beam Parameters	
Circumference [m]	78.54
Pb^{54+} rest energy [GeV]	193.7
Injection Kinetic energy [GeV/u]	0.0042
Relativistic gamma, γ_r	1.0045
Gamma transition, γ_{tr}	2.8384
Harmonic number, h	2
RF voltage [MV]	0.0011
Momentum compaction factor	0.1241
Total number of charges, N_c	2.1×10^{10}
Normalized horizontal emittance, ε_x [μm]	0.282
Normalized vertical emittance, ε_y [μm]	0.282
Bunch length, σ_z[m]	4.2

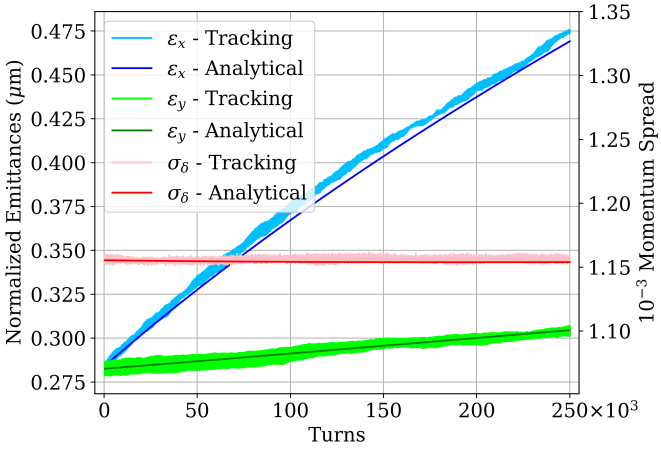

FIG. 1. Comparison of the momentum spread (red), the horizontal (blue) and vertical (green) emittances, between analytical IBS predictions (dark colors) and tracking IBS simulations (light colors), for the nominal parameters of the LEIR as described in Table I.

normalized transverse emittances of $\varepsilon_{x,y} = 0.056$ μm. The rest of the parameters remain the nominal ones. A similar comparison between the tracking simulation including the IBS kick and the analytical estimations is shown in Fig. 2. As expected, IBS becomes stronger in this case. More blow-up is produced in the horizontal plane while the momentum spread is damped more. However, good agreement is observed again. The largest discrepancy is obtained in the longitudinal plane, where the longitudinal distribution tends towards a more Gaussian shape compared to the initial binomial distribution as a result from the IBS kicks. In particular, Fig. 3 shows the initial (red) and final (blue) beam profiles as produced from the simulations (crosses) and are compared with Gaussian fits (solid lines). The difference with respect to the analytical calculations (that assume Gaussian distributions in all planes) is probably caused by the fact that the simulated distribution is not exactly Gaussian.

Figure 4 shows a comparison for the regime of short bunches. That is, the momentum spread and the bunch length in this benchmarking case are 5 times smaller than the operational ones, while in the transverse planes the beam is round

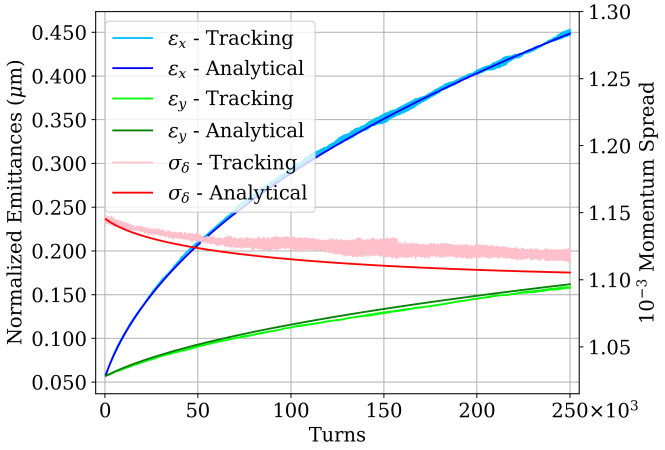

FIG. 2. Comparison of the momentum spread (red), the horizontal (blue) and vertical (green) emittances, between analytical IBS predictions (dark colors) and tracking IBS simulations (light colors), for a round beam with $\varepsilon_{x,y} = 0.056$ μm and $\sigma_z = 4.2$ m, in the LEIR.

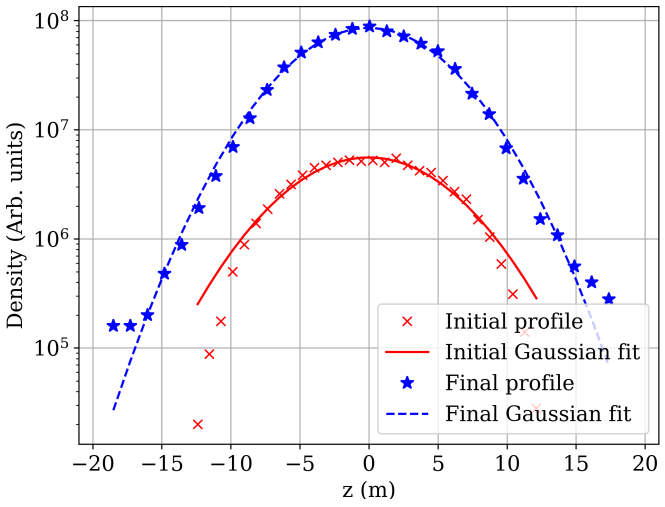

FIG. 3. Initial (red) and final (blue) longitudinal beam profiles, indicated with crosses and compared with Gaussian fits, indicated with solid lines. Tracking simulations with IBS for a round beam with $\varepsilon_{x,y} = 0.056$ μm and a bunch length of $\sigma_z = 4.2$ m.

with the nominal normalized emittances $\varepsilon_{x,y} = 0.282$ μm. In this scenario, the horizontal and the longitudinal planes experience very strong IBS effect, while the vertical emittance is slightly damped and then increased. Again, very good agreement is observed between the tracking simulations and the analytical calculations.

The last benchmarking case of the LEIR is the regime where the LEIR operates above transition. To accomplish that, the kinetic energy of the ions was increased to $E_k = 2.6075$ GeV/u, more than 600 times of the nominal one. At higher energies, the strength of the IBS effect subsides. To enhance it, in this case the transverse emittances were chosen to be very small ($\varepsilon_{x,y} \approx 0.056$ μm) to result in a sizeable horizontal emittance growth. Figure 5 shows the comparison between the tracking simulations with the IBS kicks and the analytic calculations, with these modifications. Excellent agreement between the simulation and the analytical prediction is observed. The relative difference between the analytical and the tracking simulations at the end is smaller than 2%. In this case, even though there is no growth in the longitudinal plane, some minor fluctuations can be observed. Because of the much higher energy, the synchrotron period becomes about 20000 times slower making the synchrotron oscillations of the bunch clearly visible in these results.

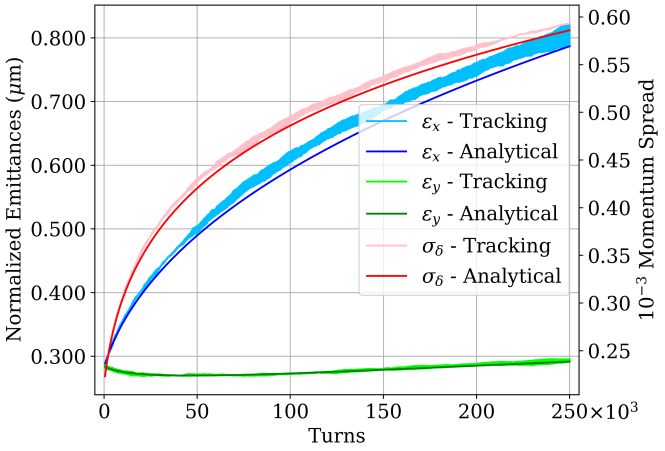

FIG. 4. Comparison of the momentum spread (red), the horizontal (blue) and vertical (green) emittances, between analytical IBS predictions (dark colors) and tracking IBS simulations (light colors), for a round beam with $\varepsilon_{x,y} = 0.282$ μm and $\sigma_z = 0.9$ m, in the LEIR.

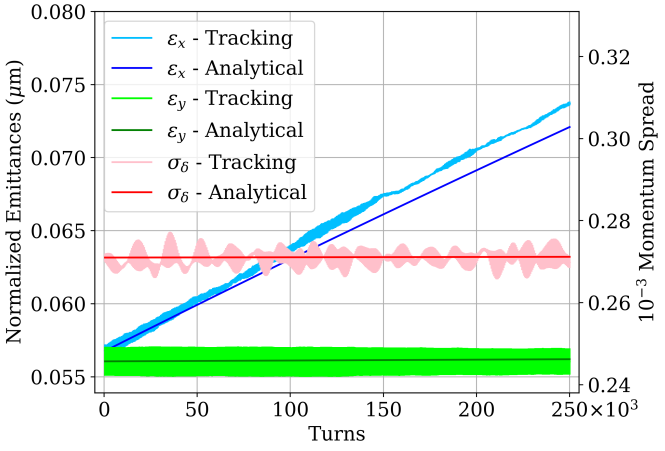

FIG. 5. Comparison of the momentum spread (red), the horizontal (blue) and vertical (green) emittances, between analytical IBS predictions (dark colors) and tracking IBS simulations (light colors), when the LEIR operates above transition with kinetic energy $E_k = 2.6075$ GeV/u for a round beam with transverse emittances $\varepsilon_{x,y} \approx 0.056$ μm.

To have a reliable IBS model, it is crucial to benchmark it successfully for different ring models with different layouts and beam parameters. In this paper, two additional benchmarking cases for the SPS are presented. The ring parameters of the SPS are shown in Table II. As before, the IBS kicks are evaluated every 500 turns according to the evolution of the

transverse beam parameters and the longitudinal line density and the total duration of the simulations is $8 \cdot 10^5$ turns, which corresponds to 20 seconds of the actual SPS cycle.

TABLE II. The SPS Parameters

Ring Parameters	
Circumference [km]	6.9
Pb^{82+} rest energy [GeV]	193.7
Injection Kinetic energy [GeV/u]	5.9
Relativistic gamma, γ_r	7.34
Gamma transition, γ_{tr}	18.14
Harmonic number, h	4653
RF voltage [MV]	3.2
Momentum compaction factor	0.1241

The first benchmarking case is for a beam with number of charges per bunch $N_c = 2.9 \times 10^{10}$, normalized transverse emittances $\varepsilon_x = 1.3$ μm, $\varepsilon_y = 0.9$ μm and a bunch length of $\sigma_z = 0.23$ m. The comparison between the tracking simulations using the modified AM (light colors) and the analytical predictions using Nagatisev's model (dark colors) is shown in Fig. 6 with the color-coding of blue for the horizontal normalized emittance, green for the vertical normalized emittance and red for the momentum spread. Very good agreement is observed in all three planes with the largest difference in the final parameters of 2% for the longitudinal plane.

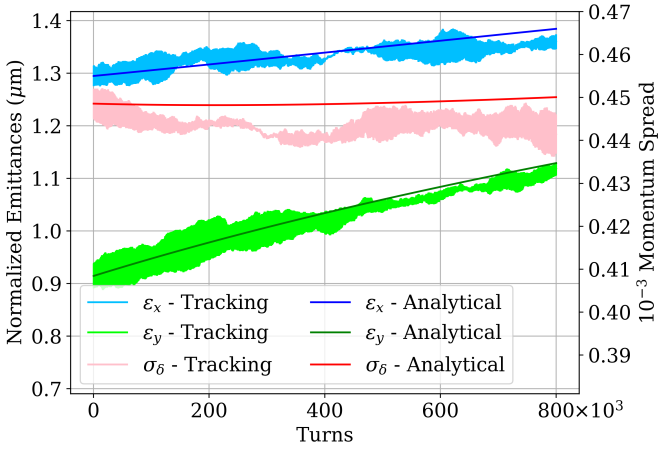

FIG. 6. Comparison of the momentum spread (red), the horizontal (blue) and vertical (green) emittances, between analytical IBS predictions (dark colors) and tracking IBS simulations (light colors) for the SPS and for initial beam parameters $\varepsilon_x = 1.3$ μm, $\varepsilon_y = 0.9$ μm and a bunch length of $\sigma_z = 0.23$ m

To further enhance the IBS effect, a second case of the SPS was done for 5 times smaller emittances than the ones mentioned above. The comparison between the tracking simulations and the analytical predictions are shown in Fig. 7, where again very good agreement is observed, despite the more severe emittance exchange between the longitudinal and transverse planes due the IBS effect. The reason for this small difference is that the longitudinal phase space was initialized as a binomial distribution, like in the case of LEIR discussed above,

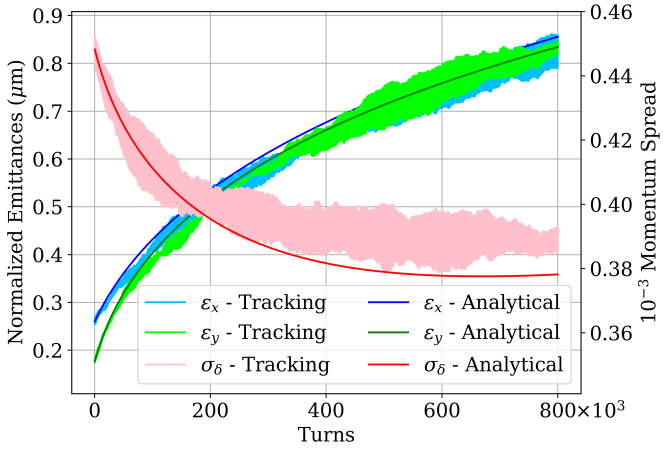

FIG. 7. Comparison of the momentum spread (red), the horizontal (blue) and vertical (green) emittances, between analytical IBS predictions (dark colors) and tracking IBS simulations (light colors) for the SPS and for initial beam parameters $\varepsilon_x = 0.26$ μm, $\varepsilon_y = 0.18$ μm and a bunch length of $\sigma_z = 0.23$ m.

and the longitudinal distribution tends towards a more Gaussian shape as a result from the IBS kicks.

Six different benchmarking cases were shown, for different regimes in the LEIR and the SPS. In all six cases, there is excellent agreement between macroparticle tracking simulations with the modified AM IBS kick and the analytical predictions using Nagaitsev's analytical IBS model. Thus, this IBS model can be tested against experimental data from machine measurements and dynamic studies that include other collective effects, such as SC. For completeness, the invariant of Piwinski [46] using this IBS kick is compared for two of these cases against the analytical predictions in Appendix B.

V. SPACE CHARGE AND INTRA-BEAM SCATTERING STUDIES IN THE LEIR

The Low Energy Ion Ring is the second accelerator and the first synchrotron of the CERN heavy ions injectors chain for the Large Hadron Collider (LHC). The main ring parameters of the LEIR are summarized in Table I, as shown earlier. LEIR's magnetic cycle has a long injection plateau during which seven beam pulses are injected from the upstream LINAC3, at a kinetic energy of 4.2 MeV/u. The seven pulses are stacked in the longitudinal phase space following an injection scheme which is based on a combined betatron and momentum phase space painting [62]. Between the individual pulses, the stored coasting beam is compressed in the 6D phase space using electron cooling. At the end of the injection phase, the beam volume reaches an equilibrium between the electron cooling and the heating processes, such as IBS and SC. When the electron cooler is turned off, the coasting beam is captured by the Radio-Frequency (RF) cavity into two bunches. Consequently, the longitudinal line density is increased due to the bunching, which in turn leads to the enhancement of the SC and IBS effects resulting in particle loss.

To understand the mechanism for these losses and how SC and IBS influences the degradation of the beam performance of the LEIR, studies were performed for different working points (WP) in controlled conditions injecting only a single pulse from LINAC3 [63]. These studies showed that the vertical emittance evolution along the duration of the magnetic cycle could not be explained by IBS only. Following up on these studies, in order to understand this discrepancy between measurements and simulations, a simulation campaign with combined IBS and SC tracking simulations was performed, to investigate the impact of the interplay between the two effects, especially in the vicinity of excited resonances, as discussed in the following.

Due to the high complexity of the machine, a set of measurements for low beam intensity (one injection), similar to [63] was chosen in order to benchmark the simulations. For these simulations, the initial parameters that were used are shown in Table III. They correspond to the measured parameters right after the end of the RF-capture.

TABLE III. Beam Parameters for the LEIR simulations

Beam Parameters	
Total number of charges, N_c	1.74×10^{10}
Normalized horizontal emittance, ε_x [μm]	0.162
Normalized vertical emittance, ε_y [μm]	0.189
Bunch length, σ_z[m]	4.5

A tune scan was performed in simulations using PyORBIT with the "frozen" potential SC kick and the ideal LEIR lattice, i.e. without machine imperfections apart from the residual lattice perturbations remaining after the compensation of the electron cooler magnetic fields. The horizontal tune was set to $Q_x = 1.82$ in all cases, while the vertical tune was varied, as indicated by the black stars in Fig. 8. For reference, the SC tune footprint was calculated for these beam parameters and is shown together with all the normal (full lines) and skew (dashed lines) systematic (red) and nonsystematic (blue) resonances up to 5^{th} order [64]. The beam distribution is initialized as Gaussian in the transverse planes and as binomial in the longitudinal plane and it consists of 5000 macroparticles, which is sufficient to perform such simulations as shown by the convergence study for SPS in the Appendix A, as well as the convergence study under extreme conditions reported in Appendix A of [36]. The aperture restrictions of the actual ring are considered [65], to accurately simulate the beam losses. Results are presented in terms of the ratio between final over initial values for intensity and transverse emittances. The initial values are measured 675 ms after the start of the magnetic cycle, while the final ones are measured 1600 ms after the start of the magnetic cycle (for comparison, the total cycle duration including the full ramp is 3600 ms, and injection takes place at 245 ms).

Even in the case of this ideal lattice, the nonlinear SC potential can drive systematic resonances of even order. In the case of the LEIR, SC simulations shown with light colors in Fig. 9, revealed four SC driven resonances: the sixth order coupling resonance $2Q_x + 4Q_y = 14$, the sixth order vertical resonance $6Q_y = 16$, the eighth order vertical resonance $8Q_y = 22$ and the fourth order coupling $2Q_x - 2Q_y = -2$ resonance [57, 66]. In these studies, we focus to the working points indicated by the grey shadowed area of the plots.

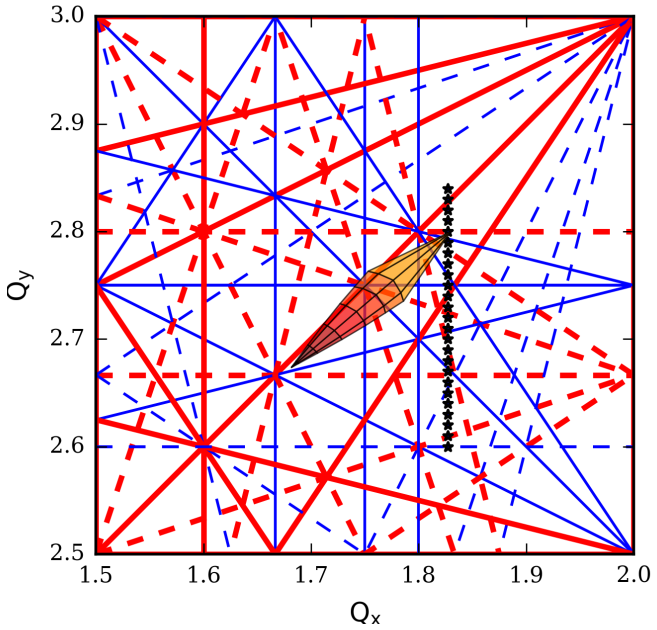

FIG. 8. Illustration of the space charge induced tune spread for the WP $(Q_x, Q_y) = (1.82, 2.80)$ in LEIR as calculated analytically for normalized emittances $\varepsilon_x = 0.16$ μm and $\varepsilon_y = 0.19$ μm, a bunch length of $\sigma_z = 4.5$ m, and an intensity $N_b = 1.6 \times 10^8$ ions. The colored rhomboid indicates the tune shift for on-momentum particles with different transverse oscillation amplitudes, as indicated by the black lines. An example of a vertical tune scan as performed in the simulations is indicated by the black stars. In addition, normal (full lines) and skew (dashed lines) systematic (red) and nonsystematic (blue) resonances are shown up to 5^{th} order.

To study the interplay between SC and IBS, IBS was included in the simulations using the modified AM described above. The results are summarized in Fig. 9 and are compared to the cases where only SC and only IBS are taken into account. It is evident that in the absence of excited resonances, IBS dominates the emittance evolution, while the interplay of the two effects clearly enhances the beam response to the resonances, resulting in larger emittance blow-up and increased particle losses.

To benchmark the combined SC and IBS simulations with experimental observations, a set of measurements of a vertical tune scan with a low intensity beam was used, as shown in Fig. 10. For this set of measurements the horizontal tune was set to $Q_x = 1.83$ and the results are presented in terms of the ratio of final over initial values of the transverse emittances and the intensity. As before, the initial values are measured 675 ms after the start of the magnetic cycle, i.e. the end of the RF-capture, while the final ones are measured 1600 ms after the start of the magnetic cycle. For each measurement a fresh beam was injected.

Due to the low lattice periodicity (2-fold) of the LEIR and

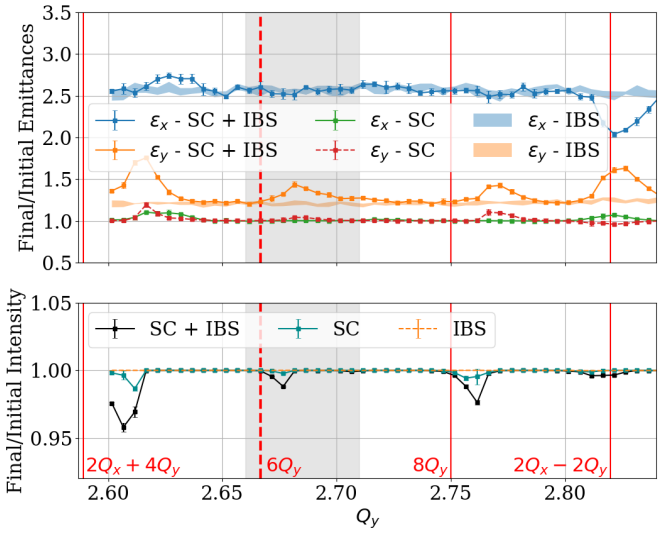

FIG. 9. SC and IBS simulations versus combined SC with IBS simulations comparison of the final over initial values of the horizontal (green, dashed blue and solid blue, respectively) and vertical (red, dashed orange and solid orange) emittances (top) and intensity (bottom) for the ideal lattice of LEIR. The error-bars are indicated by the standard deviation over three different runs.

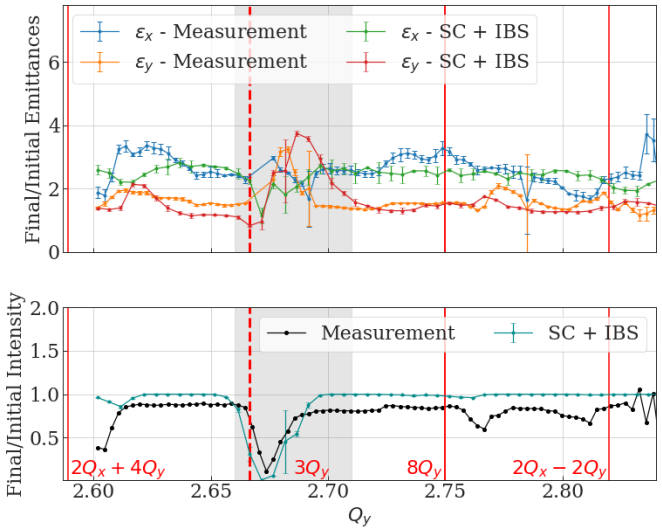

FIG. 10. Measurements in LEIR versus combined SC and IBS simulations comparison of the final over initial values of the horizontal (blue and green, respectively) and vertical (orange, red) emittances (top) and intensity (bottom). The error-bars are indicated by the standard deviation over three different runs.

due to random magnetic errors, various resonances are observed to be excited in the measurements, including the third order vertical $3Q_y = 8$ and the third order coupling $Q_x+2Q_y = 7$ resonances. Attempts have been made to compensate the $3Q_y = 8$ resonance by using two independently powered skew sextupole correctors with the appropriate phase advance [63]. The compensation was optimised by maximizing the beam transmission while crossing the excited resonance dynamically. The results are shown in Fig. 11 in terms of the current of the skew sextupoles and the resulting beam transmission during the resonance crossing. Corrector settings could be found that restore a beam transmission of more than 90% compared to 30% without compensation.

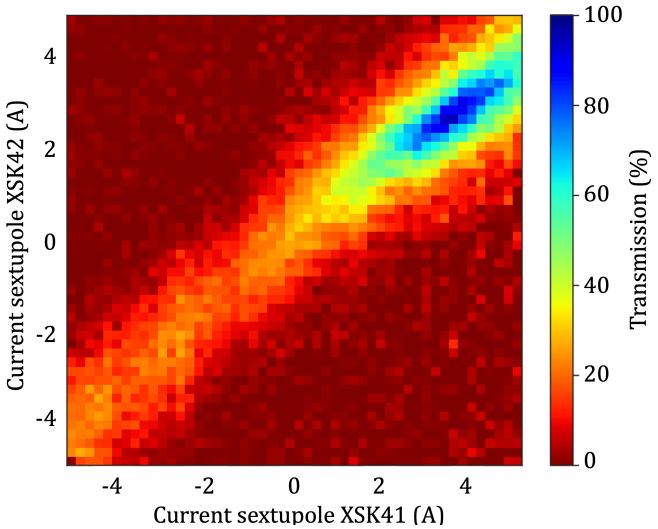

FIG. 11. Beam transmission in LEIR while crossing the $3Q_y = 8$ resonance as a function of the currents in the skew sextupoles [63].

To re-create the uncompensated resonance of the experiment in the simulation study, skew sextupole errors were added in the ideal lattice to excite the $3Q_y$ resonance. A suitable error for this case is to use the optimal settings of the skew sextupole correctors that compensate the $3Q_y$ resonance in the real machine, but with inverted polarity. This error mostly affects the $3Q_y$ resonance and thus will have similar behavior between simulations and measurements.

Combined simulations of IBS and SC were performed using this configuration for a horizontal tune of $Q_x = 1.83$ and a similar simulation duration as the 925 ms time window of the measurements. For clarity, simulations with only SC and only IBS are ignored in this case. The macroparticle distribution was again initialized as Gaussian in the transverse planes and binomial in the longitudinal plane, consisting of 5000 macroparticles. The results are presented in Fig. 10 in comparison with the measurements. Quite good agreement is achieved around the $3Q_y = 8$ resonance and for vertical tunes that are not affected by other resonances. However, in the real machine there seem to be errors exciting additional resonances in the measurements that do not clearly appear in the simulation. Thus, these resonances seem not to be caused by the space charge potential itself, but rather from additional unknown magnetic errors present in the ring, but not reflected in the corresponding model.

VI. SPACE CHARGE AND INTRA-BEAM SCATTERING STUDIES FOR THE SPS

The SPS is the largest accelerator of the LHC ion injector chain, with a circumference of around 7 km. A more detailed

list of parameters was shown earlier in Table II. Despite the thousandfold higher kinetic energy of the Pb ion beam at the SPS injection compared to the LEIR injection, SC induces a considerable tune shift of $\Delta Q_{x,y} = (-0.2, -0.29)$ due to the short bunch length and the large machine circumference, making the beam susceptible to resonances.

In the operational conditions of 2016, an emittance exchange between horizontal and vertical planes, followed by a large emittance blow up in both planes was observed along the flat bottom of the SPS acceleration cycle, as shown in Fig. 12 (lines with point markers). A campaign of standalone IBS and SC simulations was performed in 2020 [67] as an attempt to explain the behavior of the observed emittance evolution. The results of the SC simulation shown in solid lines with error bars and the IBS analytical calculations using Nagaitsev's method in light colors, are also shown in Fig. 12. It is evident that the observed emittance behavior cannot be explained neither from standalone SC or IBS simulations.

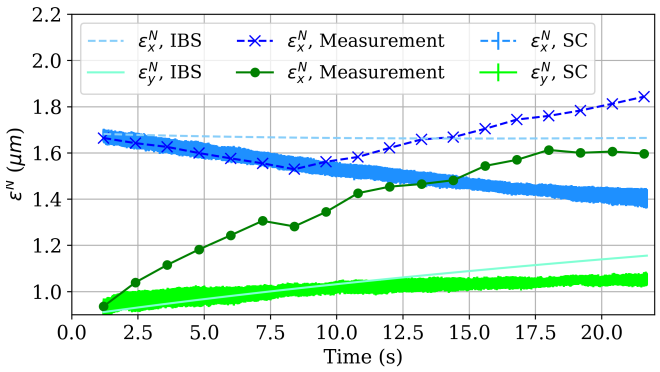

FIG. 12. Evolution of the horizontal (blue) and vertical (green) emittance as observed in operation (dotted lines), from IBS analytical calculations using the Nagaitsev's method (light colors) and from SC simulations (solid line with errorbars) in PyORBIT (averaged over 3 different runs). The error bars correspond to the one standard deviation.

To this end, a simulation campaign was initiated to investigate the impact of the interplay between SC and IBS and whether this interplay could explain the observed emittance behavior. The simulations were performed using the same configuration as for LEIR, with the difference that the SC potential is re-evaluated every 1000 turns based on the evolution of the tracked particles. Additionally, the coefficients of the IBS kicks are evaluated every 1000 turns, while each particle receives a change in its momenta depending on the beam parameters and the particle's longitudinal position at every turn.

The generated initial distribution is Gaussian in all planes and comprises 1000 macroparticles—a necessary compromise given the high complexity of these simulations, yet sufficient as demonstrated in the convergence studies in Appendix A. In addition, a quadrupolar error is included in the ideal lattice, inducing a 5–10% beta-beating, similar to what is observed in the real machine under operational conditions. To accurately simulate the beam losses, the realistic physical aperture of the SPS is taken into account in the simulations [68].

Using the aforementioned setup, a combined simulation with SC and IBS was performed. Figure 13 shows the evolution of the normalized horizontal (blue) and vertical (green) emittances in time, as observed from the measurements (lines with point markers) and as predicted by the combined simulations (solid line). For the first time, a good agreement could be achieved in both planes, demonstrating the importance of the interplay between the two effects in this case. In the vertical plane the agreement is truly excellent while, in the horizontal plane some minor discrepancy is observed in the trend of the evolution. It has to be noted that the experimentally observed particle losses were of the order of 10 % and they were not recreated in these simulations, which might explain the slightly larger emittance growth. Although no data were stored for the evolution of the longitudinal beam profile during these measurements, there is typically a reduction in bunch length observed experimentally. In contrast, in the simulations presented here there is instead an increase of the bunch length by about 6 %. These differences need to be addressed in more detail in future studies.

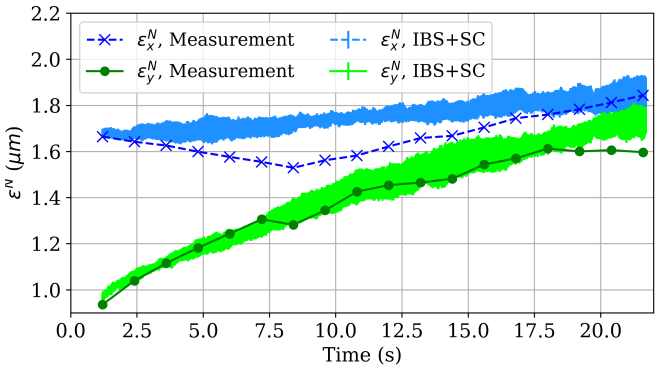

FIG. 13. Evolution of the horizontal (blue) and vertical (green) emittance as observed in operation (dotted lines) and from combined SC and IBS simulations (solid line with errorbars) in PyORBIT (averaged over 3 different runs). The error bars correspond to the one standard deviation.

VII. CONCLUSIONS AND FUTURE PLANS

In this paper, an IBS kick was implemented in a tracking code, to study the interplay between SC and IBS in the context of the LEIR and SPS accelerators for Pb ion beams. Both accelerators operate below transition which makes the implementation of IBS in tracking simulations not trivial.

The existing IBS approximate model based on the kinetic theory of gases, implemented by Zenkevich, Bolshakov and Boine-Frankenheim, is capable of simulating the IBS effect in macroparticle tracking simulations using significantly smaller number of macroparticles compared to the BCM model, which requires a large number of macroparticles to sufficiently populate all the cells. Inspired by this model, a more general extension is presented in this publication that is able to simulate the IBS effect for a wider range of accelerators, using the formal-

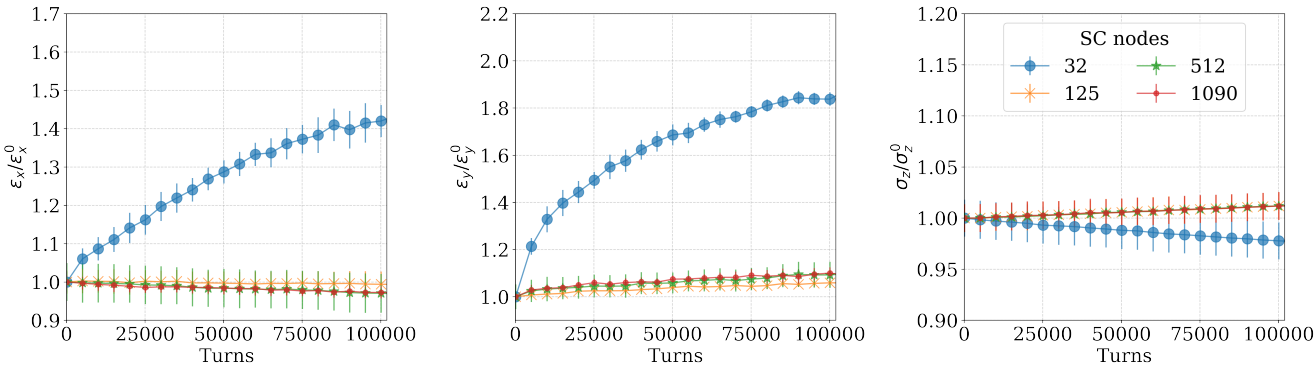

FIG. 14. Evolution of the normalized horizontal emittance (left), vertical emittance (center) and momentum spread (right), for 1000 macroparticles, for four different numbers of SC nodes around the SPS lattice. The error-bars correspond to the standard deviation over three different simulations.

ism of Nagaitsev and including the longitudinal line density to modulate the kicks for the particles according to their longitudinal position along the longitudinal profile. Benchmarking cases for the LEIR and the SPS are presented, for different parameter regimes. All benchmarking cases show excellent agreement with the analytical predictions of IBS.

For the case of the LEIR, standalone SC and IBS simulations as well as simulations combining both effects were performed using the ideal lattice (i.e. without machine imperfections). In the LEIR, several SC driven resonances are excited due to the low lattice periodicity and the nonlinear potential from SC for a Gaussian transverse distribution. The combined simulations show a clear enhancement of the particles' response to the resonances, leading to larger emittance blow-up and increased particle losses. An attempt was made to compare the combined simulations with experimental data by adding an error to the ideal lattice in the simulations to excite the $3Q_y$ resonance, equivalent to the residual nonlinear error remaining after the correction applied in the real machine to compensate it. The comparison between these simulations and the measurements in which the $3Q_y = 8$ resonance is uncompensated, revealed that the interplay of IBS and SC can explain very well the emittance behavior in both transverse planes for the tunes that are mostly affected from the present resonance components. In addition, particle losses appear to be generally larger for all working points in the real machine.

For the SPS, standalone SC and IBS simulations as well as combined simulations were performed in the presence of a quadrupolar errors to induce a 5-10% beta-beating, similar to what is observed in the real ring, in operational conditions. The standalone simulations of SC and IBS could not explain the beam behavior that was observed in the measurements of 2016. On the contrary, the combined simulations of SC and IBS produced promising results, explaining for the first time the experimental observations from 2016, revealing the importance of the interplay between SC and IBS effects.

Our study shows that the interplay of SC and IBS effects need to be taken into account in order to reproduce experimental observations of beam degradation close to lattice resonances for both the LEIR and the SPS. In addition, a good knowledge of the lattice imperfections in both rings is important for obtaining an accurate performance prediction and optimization.

ACKNOWLEDGMENTS

The authors would like to thank N. Biancacci and the other members of the LEIR team at CERN for the insight and the support given during the machine experiments, and A. Latina for fruitful discussions.

Appendix A: Convergence studies

Choosing the appropriate number of SC kicks around the lattice of the ring and the number of macroparticles in tracking simulations is crucial to minimize computational resources without sacrificing accuracy. To address this, a convergence study was performed for two cases. These cases involved scanning different numbers of SC kicks or macroparticles in the SPS to determine the optimal parameters. The ideal lattice of SPS was used for both study cases, including a quadrupolar error that induces a 5-10% beta-beating, with the initial beam parameters similar to those in Sec. VI. The duration of the simulations corresponds to 100000 turns around the SPS ring.

In the first case, the number of SC kicks around the ring was varied, with the distribution initialized using 1000 macroparticles for all cases. Figure 14 presents the transverse emittances and momentum spread, normalized to their initial values, for 32, 125, 512, and 1090 SC nodes. These values correspond to approximately 0.005, 0.02, 0.075, and 0.16 SC nodes per meter around the ring, or 1.25, 5, 20, and 42 SC nodes per betatron wavelength, respectively, based on the integer part of the transverse tunes of $Q = 26$.

The results indicate that only the case with the smallest number of SC nodes (32) shows a significant divergence from the other three scenarios. While the case with 125 SC nodes ex-

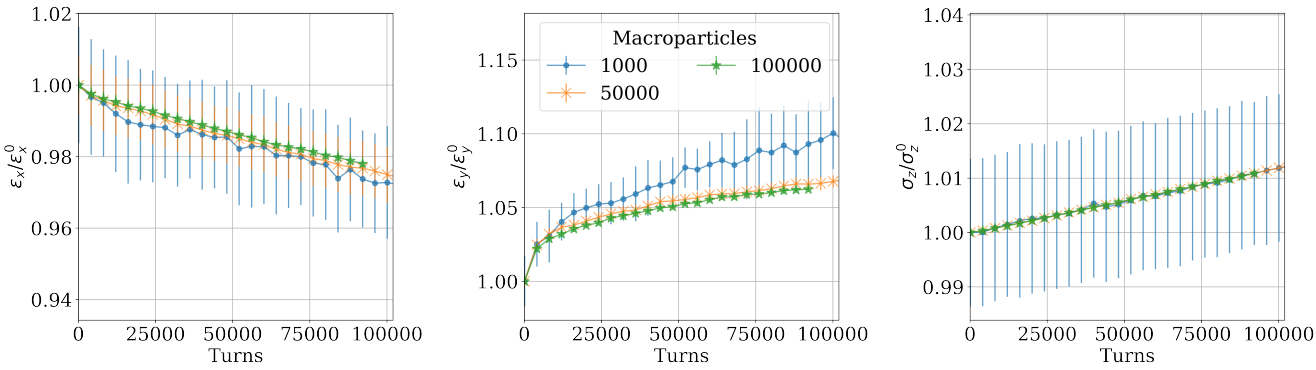

FIG. 15. Evolution of the normalized horizontal emittance (left), vertical emittance (center) and momentum spread (right), for 1090 SC nodes around the SPS lattice, for three different numbers of macroparticles.The error-bars correspond to the standard deviation over three different simulations.

hibits a slight deviation from the two cases with larger numbers of SC nodes, it remains within acceptable limits. The cases with 512 and 1090 SC nodes show complete agreement with each other. Moreover, increasing the number of SC nodes does not significantly impact the simulation runtime. Therefore, 1090 SC nodes were selected for all subsequent studies in the SPS.

In the second study, the number of macroparticles was varied while the number of SC nodes was fixed at 1090. Figure 15 shows the transverse emittances and momentum spread, normalized to their initial values, for distributions initialized with 1000, 50000, and 100000 macroparticles. In the horizontal and longitudinal planes, all three cases agree perfectly, although the standard deviation over three different simulations is noticeably larger for the case of 1000 macroparticles. In the vertical plane, the two cases with larger numbers of macroparticles agree very well, while the case with 1000 macroparticles shows a 3% difference, with error bars covering this margin. Therefore, a distribution with 1000 macroparticles is sufficient to produce accurate results while significantly reducing the simulation run time.

Appendix B: Piwinski's invariant

Following Piwinski's model [46], there is an invariant quantity given by the equation:

$$\langle H \rangle \left(\frac{1}{\gamma_r^2} - \frac{1}{\gamma_{tr}^2} \right) + \frac{\langle \varepsilon_x \rangle}{\beta_x} + \frac{\langle \varepsilon_y \rangle}{\beta_y} = \text{const.}, \tag{B1}$$

where H is the longitudinal invariant. This equation shows that the behavior of particles under the influence of IBS is different when the ring operates below or above transition. Above transition ($\gamma_r > \gamma_{tr}$), the coefficient of H is negative and the oscillation energy can increase indefinitely as long as it does not exceed other limitations. This means that no actual equilibrium can exist in the presence of IBS alone.

Below transition ($\gamma_r < \gamma_{tr}$), all three coefficients are positive and their oscillation energy is bounded. Thus, equilibrium can exist by the redistribution of the momenta among the three planes. This means that in the below transition case, in one or more planes emittance damping can be observed.

To test the accuracy of this theory, two cases from the benchmarking examples of LEIR and the SPS were selected. The Piwinski invariant was computed, along with the evolution of the emittances, over the duration of the simulation. For simplicity, the invariant was calculated using Eq. (30) from [69], and analytical IBS predictions were used to avoid fluctuations caused by the statistical nature of macroparticle simulations.

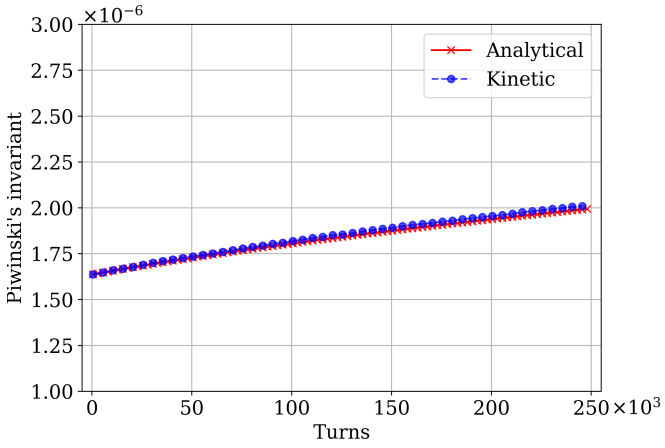

FIG. 16. Piwinski's invariant, as calculated from the macroparticle tracking results using the introduced Kinetic kick (blue), and the results from analytical predictions (red) corresponding to the case shown in Fig. 1, starting from the nominal parameters of LEIR as described in Table I.

The first case, shown in Fig. 16, corresponds to the simulation in Fig. 1, where the nominal parameters of LEIR, as described in Table I, were used. This is a below-transition case, where slight damping in the longitudinal plane was observed, along with growth in the transverse planes. The comparison of the total Piwinski invariants between the macroparticle tracking simulations (blue) and the analytical calcula-

tions (red) show excellent agreement. Evidently, the Piwinski invariant does not remain constant but instead follows an increasing trend in both cases. This behavior is expected since the model assumes the "smooth" lattice approximation while, in reality, the derivatives of the beta and dispersion functions, β'_x and η'_x, have non-zero values in LEIR [70].

The second case corresponds to Fig. 6, where the beam is initialized with transverse emittances of $\varepsilon_x = 1.3$ μm and $\varepsilon_y = 0.9$ μm, and a bunch length of $\sigma_z = 0.23$ m. Figure 17 compares the total Piwinski invariants from macroparticle tracking simulations (blue) and analytical IBS predictions using Nagaitsev's formalism (red), showing good agreement. The invariant calculation is highly sensitive to statistical fluctuations in beam sizes, leading to minor discrepancies, which are negligible relative to the scale of the vertical axis. Similar to the previous case, an increase in the invariant is observed, which is attributed to the non-zero derivatives of the beta and dispersion functions, β'_x and η'_x.

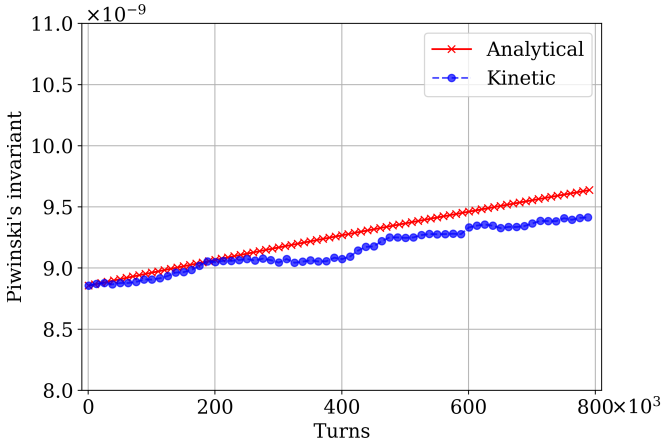

FIG. 17. Piwinski's invariant, as derived from the macroparticle tracking results using the introduced Kinetic kick (blue), is compared with the analytical predictions (red) for the case depicted in Fig. 6. This case involves a Pb-ion beam initialized with transverse emittances of $\varepsilon_x = 1.3$ μm and $\varepsilon_y = 0.9$ μm, and a bunch length of $\sigma_z = 0.23$ m, in the SPS.

[1] T. Mertens, *Intrabeam scattering in the LHC*, Master's thesis, Porto U. (2011), presented 17 Jun 2011.

[2] J. Wei, A. Fedotov, W. Fischer, N. Malitsky, G. Parzen, and J. Qiang, Intra-beam Scattering Theory and RHIC Experiments, AIP Conference Proceedings **773**, 389 (2005).

[3] W. Fischer, M. Bai, M. Blaskiewicz, J. M. Brennan, P. Cameron, R. Connolly, A. Lehrach, G. Parzen, S. Tepikian, K. Zeno, and J. Van Zeijts, Measurements of Intrabeam scattering growth times with gold beam below transition in RHIC, Conf. Proc. C **0106181**, 2857 (2001).

[4] R. Bruce, J. M. Jowett, M. Blaskiewicz, and W. Fischer, Time evolution of the luminosity of colliding heavy-ion beams in BNL Relativistic Heavy Ion Collider and CERN Large Hadron Collider, Phys. Rev. ST Accel. Beams **13**, 091001 (2010).

[5] V. Lebedev, Single and Multiple Intrabeam Scattering in Hadron Colliders, AIP Conference Proceedings **773**, 440 (2005).

[6] S. Papadopoulou, F. Antoniou, T. Argyropoulos, M. Hostettler, Y. Papaphilippou, and G. Trad, Impact of non-Gaussian beam profiles in the performance of hadron colliders, Phys. Rev. Accel. Beams **23**, 101004 (2020).

[7] P. S. Papadopoulou, *Bunch characteristics evolution for lepton and hadron rings under the influence of the Intra-beam scattering effect*, Ph.D. thesis, University of Crete (2019).

[8] V. A. Lebedev, I. Lobach, A. Romanov, and A. Valishev, *Report on Single and Multiple Intrabeam Scattering Measurements in IOTA Ring in Fermilab*, Tech. Rep. (Fermi National Accelerator Lab., Batavia, IL (United States), 2020).

[9] F. Antoniou, *Optics design of Intrabeam Scattering dominated damping rings*, Ph.D. thesis, National Technical University of Athens (2012).

[10] F. Antoniou, Y. Papaphilippou, M. Aiba, M. Boege, N. Milas, A. Streun, and T. Demma, Intrabeam scattering studies at the Swiss light source, in *Proc. 2nd International Particle Accelerator Conference (IPAC'12)* (New Orleans, Louisiana, USA, 2012) pp. 1951–1953.

[11] K. L. F. Bane, *Intra-Beam Scattering, Impedance, and Instabilities in Ultimate Storage Rings*, Tech. Rep. (SLAC National Accelerator Lab., Menlo Park, CA (United States), 2012).

[12] K. L. F. Bane, H. Hayano, K. Kubo, T. Naito, T. Okugi, and J. Urakawa, Intrabeam scattering analysis of measurements at KEK's Accelerator Test Facility damping ring, Physical Review Special Topics - Accelerators and Beams **5**, 10.1103/physrevstab.5.084403 (2002).

[13] K. Kubo, S. K. Mtingwa, and A. Wolski, Intrabeam scattering formulas for high energy beams, Phys. Rev. ST Accel. Beams **8**, 081001 (2005).

[14] Z. Huang, *Intrabeam scattering in an X-ray FEL driver*, Tech. Rep. (SLAC National Accelerator Lab., Menlo Park, CA (United States), 2002).

[15] A. Xiao and M. Borland, Intrabeam Scattering Effect Calculated for a Non-Gaussian Distributed Linac Beam, in *Proc. PAC'09* (2010) pp. 3281–3283.

[16] S. D. Mitri, G. Perosa, A. Brynes, I. Setija, S. Spampinati, P. H. Williams, A. Wolski, E. Allaria, S. Brussaard, L. Giannessi, G. Penco, P. R. Rebernik, and M. Trovò, Experimental evidence of intrabeam scattering in a free-electron laser driver, New Journal of Physics **22**, 083053 (2020).

[17] J. Hunt, C. Carli, J. Resta-López, and C. Welsch, Emittance measurements in low energy ion storage rings, Nuclear Instruments and Methods in Physics Research Section A: Accelerators, Spectrometers, Detectors and Associated Equipment **896**, 139 (2018).

[18] A. Fedotov, M. Bai, M. M. Blaskiewicz, W. Fischer, D. Kayran, C. Montag, T. Satogata, S. Tepikian, and G. Wang, Beam lifetime and limitations during low-energy RHIC operation, in *Proc. PAC'11*, Particle Accelerator Conference (2011) pp. 2285–2287.

[19] M. R. F. Siggel-King, C. P. Welsch, A. I. Papash, and A. V.

Smirnov, Long Term Beam Dynamics in Ultra-Low Energy Storage Rings, Conf. Proc. C **110904**, 2166 (2011).

[20] G. Franchetti, I. Hofmann, M. Giovannozzi, M. Martini, and E. Metral, Space charge and octupole driven resonance trapping observed at the CERN Proton Synchrotron, Phys. Rev. ST Accel. Beams **6**, 124201 (2003).

[21] E. Métral, G. Franchetti, M. Giovannozzi, I. Hofmann, M. Martini, and R. Steerenberg, Observation of octupole driven resonance phenomena with space charge at the CERN Proton Synchrotron, Nuclear Instruments and Methods in Physics Research Section A: Accelerators, Spectrometers, Detectors and Associated Equipment **561**, 257 (2006), proceedings of the Workshop on High Intensity Beam Dynamics.

[22] G. Franchetti, O. Chorniy, I. Hofmann, W. Bayer, F. Becker, P. Forck, T. Giacomini, M. Kirk, T. Mohite, C. Omet, A. Parfenova, and P. Schütt, Experiment on space charge driven nonlinear resonance crossing in an ion synchrotron, Phys. Rev. ST Accel. Beams **13**, 114203 (2010).

[23] G. Franchetti, S. Gilardoni, A. Huschauer, F. Schmidt, and R. Wasef, Space charge effects on the third order coupled resonance, Phys. Rev. Accel. Beams **20**, 081006 (2017).

[24] F. Asvesta, H. Bartosik, S. Gilardoni, A. Huschauer, S. Machida, Y. Papaphilippou, and R. Wasef, Identification and characterization of high order incoherent space charge driven structure resonances in the CERN Proton Synchrotron, Phys. Rev. Accel. Beams **23**, 091001 (2020).

[25] A. Saá Hernández, H. Bartosik, N. Biancacci, S. Hirlaender, A. Huschauer, and D. Moreno Garcia, Space Charge Studies on LEIR, J. Phys. Conf. Ser. **1067**, 062020 (2018).

[26] R. Ainsworth, P. Adamson, J. Amundson, I. Kourbanis, Q. Lu, and E. Stern, High intensity space charge effects on slip stacked beam in the Fermilab Recycler, Phys. Rev. Accel. Beams **22**, 020404 (2019).

[27] V. Shiltsev, Space-Charge and Other Effects in Fermilab Booster and IOTA Rings' Ionization Profile Monitors, in *Proc. IBIC'21*, International Beam Instrumentation Conference No. 10 (JACoW Publishing, Geneva, Switzerland, 2021) pp. 193–197, https://doi.org/10.18429/JACoW-IBIC2021-TUPP05.

[28] Y. Alexahin and V. Kapin, On possibility of space-charge compensation in the Fermilab Booster with multiple electron columns, Journal of Instrumentation **16** (03), P03049.

[29] M. Chung, V. Shiltsev, and L. Prost, Space-Charge Compensation for High-Intensity Linear and Circular Accelerators at Fermilab, in *1st North American Particle Accelerator Conference* (Pasadena, CA, USA, 2013).

[30] G. Dell and S. Peggs, Simulation of the space charge effect in RHIC, in *Proceedings Particle Accelerator Conference*, Vol. 4 (Dallas, TX, USA, 1995) pp. 2327–2329.

[31] V. N. Litvinenko and G. Wang, Compensating tune spread induced by space charge in bunched beams, Phys. Rev. ST Accel. Beams **17**, 114401 (2014).

[32] M. Venturini, K. Oide, and A. Wolski, Space charge and equilibrium emittances in damping rings, Conf. Proc. C **060626**, 882 (2006).

[33] M. Venturini and K. Oide, *Direct space charge effects on the ILC damping rings: Task force report*, Tech. Rep. (Lawrence Berkeley National Laboratory (LBNL), Berkeley, CA (United States), 2006).

[34] M. Venturini, *Space-Charge Effects in the Super B-Factory LER*, Tech. Rep. (Lawrence Berkeley National Laboratory (LBNL), Berkeley, CA (United States), 2007).

[35] A. Xiao, M. Borland, L. Emery, Y. Wang, and K. Y. Ng, Direct Space Charge Calculation in Elegant and Its Application to the ILC Damping Ring, Conf. Proc. C **070625**, 3456 (2007).

[36] M. Zampetakis, F. Antoniou, F. Asvesta, H. Bartosik, and Y. Papaphilippou, Interplay of space charge, intrabeam scattering, and synchrotron radiation in the Compact Linear Collider damping rings, Phys. Rev. Accel. Beams **27**, 064403 (2024).

[37] N. Alekseev, A. Bolshakov, E. Mustafin, and P. Zenkevich, Numerical code for Monte-Carlo simulation of ion storage, AIP Conference Proceedings **480**, 31 (1999), https://pubs.aip.org/aip/acp/article-pdf/480/1/31/11636089/31_1_online.pdf.

[38] A. Vivoli and M. Martini, Intra-Beam Scattering in the CLIC Damping Rings, in *Proc. IPAC'10*, International Particle Accelerator Conference No. 1 (2010) pp. 3557–3559.

[39] M. Biagini, M. Boscolo, T. Demma, A. Chao, K. Bane, and M. Pivi, Multiparticle simulation of intrabeam scattering for superb, in *Proc. IPAC'11*, International Particle Accelerator Conference No. 2 (2011) pp. 2259–2261.

[40] M. T. F. Pivi, CMAD: A new self-consistent parallel code to simulate the electron cloud build-up and instabilities, Conf. Proc. C **070625**, 3636 (2007).

[41] K. G. Sonnad, F. Antoniou, Y. Papaphilippou, K. S. B. Li, M. Boscolo, T. Demma, A. Chao, C. H. Rivetta, and M. T. F. Pivi, Multi-Particle Simulation Codes Implementation to Include Models of a Novel Single-bunch Feedback System and Intra-beam Scattering, Conf. Proc. C **1205201**, 3147 (2012).

[42] P. Zenkevich, O. Boine-Frankenheim, and A. Bolshakov, A new algorithm for the kinetic analysis of intra-beam scattering in storage rings, Nuclear Instruments and Methods in Physics Research Section A: Accelerators, Spectrometers, Detectors and Associated Equipment **561**, 284 (2006).

[43] P. Zenkevich, A. Bolshakov, and O. Boine-Frankenheim, Kinetic effects in multiple intra-beam scattering, AIP Conf. Proc. **773**, 425 (2005).

[44] A. Bolshakov and P. Zenkevich, Numerical modeling of intrabeam scattering of particles in ring accelerators and storage rings by approximate solution of the fokker–planck equation in the space of invariants, Atomic Energy **112**, 170 (2012).

[45] H. Risken, Fokker-planck equation, in *The Fokker-Planck Equation: Methods of Solution and Applications* (Springer Berlin Heidelberg, Berlin, Heidelberg, 1996) pp. 63–95.

[46] A. Piwinski, Intra-beam-Scattering, in *9th International Conference on High-Energy Accelerators* (1974) pp. 405–409.

[47] S. Nagaitsev, Intrabeam scattering formulas for fast numerical evaluation, Phys. Rev. ST Accel. Beams **8**, 064403 (2005).

[48] J. D. Bjorken and S. K. Mtingwa, Intrabeam scattering, Part. Accel. **13**, 115 (1982).

[49] M. Conte and M. Martini, Intrabeam Scattering in the CERN Anti-Proton Accumulator, Part. Accel. **17**, 1 (1985).

[50] F. Antoniou and F. Zimmermann, *Revision of Intrabeam Scattering with Non-Ultrarelativistic Corrections and Vertical Dispersion for MAD-X*, Tech. Rep. (CERN, Geneva, Switzerland, 2012).

[51] M. Blaskiewicz and J. M. Brennan, Bunched Beam Stochastic Cooling Simulations and Comparison with Data, Conf. Proc. C **07091010**, 125 (2007).

[52] M. Blaskiewicz, J. M. Brennan, and F. Severino, Operational stochastic cooling in the relativistic heavy-ion collider, Phys. Rev. Lett. **100**, 174802 (2008).

[53] Carlson, B. C., Three Improvements in Reduction and Computation of Elliptic Integrals, Journal of research of the National Institute of Standards and Technology **105(5)**, 413 (2002).

[54] F. Schmidt, E. Forest, and E. McIntosh, *Introduction to the polymorphic tracking code: Fibre bundles, polymorphic Taylor types and "Exact tracking"*, Tech. Rep. (CERN, Geneva, Switzerland, 2002).

[55] A. Shishlo, S. Cousineau, J. Holmes, and T. Gorlov, The Particle Accelerator Simulation Code PyORBIT, Procedia Computer Science **51**, 1272 (2015), international Conference On Computational Science, ICCS 2015.

[56] A. Shishlo, S. Cousineau, V. Danilov, J. Galambos, S. Henderson, and J. Holmes, The ORBIT simulation code: benchmarking and applications, in *Proc. ICAP 2006* (Chamonix, France, 2006) pp. 53–58.

[57] F. Asvesta, *Space charge and lattice driven resonances at the CERN injectors.*, Ph.D. thesis, National Technical University of Athens (2020).

[58] F. Schmidt, Y. Alexahin, J. Amundson, H. Bartosik, G. Franchetti, J. Holmes, A. Huschauer, V. Kapin, A. Oeftiger, E. Stern, and M. Titze, Code bench-marking for long-term tracking and adaptive algorithms, in *Proc. of ICFA Advanced Beam Dynamics Workshop on High-Intensity and High-Brightness Hadron Beams (HB'16)* (Malmö, Sweden, 2016) pp. 357–361.

[59] R. Li, T. Sen, and J.-F. Ostiguy, Modeling Transverse Space Charge effects in IOTA with pyORBIT (2021), arXiv:2106.03327 [physics.acc-ph].

[60] Y. Yuan, *Space-charge driven transverse beam instabilities in synchrotrons*, Ph.D. thesis, Technische Universität, Darmstadt (2018).

[61] M. Bassetti and G. A. Erskine, *Closed expression for the electrical field of a two-dimensional Gaussian charge*, Tech. Rep. (CERN, Geneva, Switzerland, 1980).

[62] O. S. Brüning, P. Collier, P. Lebrun, S. Myers, R. Ostojic, J. Poole, and P. Proudlock, *LHC Design Report*, CERN Yellow Reports: Monographs (CERN, Geneva, Switzerland, 2004).

[63] A. Saá Hernández, H. Bartosik, N. Biancacci, S. Hirlaender, D. Moreno, and M. Zampetakis, Detailed Characterisation of the LEIR Intensity Limitations for a Pb Ion Beam, in *Proc. 10th International Particle Accelerator Conference (IPAC'19)* (Melbourne, Australia, 2019) pp. 3196–3199.

[64] F. Asvesta and H. Bartosik, *Resonance Driving Terms From Space Charge Potential*, Tech. Rep. (CERN, Geneva, Switzerland, 2019).

[65] Low Energy Ion Ring Optics Repository, `https://acc-models.web.cern.ch/acc-models/leir/` (2021).

[66] F. Asvesta, F. Antoniou, H. Bartosik, G. P. Di Giovanni, and Y. Papaphilippou, Coupling and Space Charge Studies at the CERN PSB, in *Proc. 10th International Particle Accelerator Conference (IPAC'19)* (Melbourne, Australia, 2019) pp. 3192–3195.

[67] I. John and H. Bartosik, *Space charge and intrabeam scattering effects for Lead-ions and Oxygen-ions in the LHC injector chain*, Tech. Rep. (CERN, Geneva, Switzerland, 2021).

[68] Super Proton Synchrotron Optics Repository, `https://acc-models.web.cern.ch/acc-models/sps/` (2021).

[69] M. Martini, F. Antoniou, and Y. Papaphilippou, Intrabeam Scattering, ICFA Beam Dyn. Newslett. **69**, 38 (2016).

[70] A. Piwinski, J. D. Bjorken, and S. K. Mtingwa, Wilson prize article: Reflections on our experiences with developing the theory of intrabeam scattering, Phys. Rev. Accel. Beams **21**, 114801 (2018).